Desalination and Water Treatment
www.deswater.com

doi: 10.5004/dwt.2021.27460

231 (2021) 244–253
August

Novel Fe_3O_4@PPy/TCPP nanocomposite as a superior adsorbent for elimination of toxic Hg(II) and dye pollutants

Javad Shokraiyan[a], Meisam Asadi[b], Vahdat Jahed[a], Taghi Sahraeian[c], Mahboubeh Rabbani[b,*]

[a]*Department of Chemistry and Biochemistry, Ohio University, Athens, Ohio 45701, USA, emails: js785716@ohio.edu (J. Shokraiyan), Vj547816@ohio.edu (V. Jahed)*
[b]*Department of Chemistry, Iran University of Science and Technology, Tehran 16846-13114, Iran, Tel. +98-21-77240290; Fax: +98-21-77491204; emails: m_rabani@iust.ac.ir (M. Rabbani), meisamasadi2020@gmail.com (M. Asadi)*
[c]*Department of Chemistry and Biochemistry, Ohio State University, Columbus, Ohio 43210, USA, email: Sahraeian.1@buckeyemail.osu.edu*

Received 31 October 2020; Accepted 18 May 2021

ABSTRACT

Herein, the synthesis of functionalized polymer microspheres core-shell structure is successfully fabricated by a process involving three steps: (1) preparation of superparamagnetic Fe_3O_4 nanoparticles through a co-precipitation method, (2) Fe_3O_4 nanoparticles were functionalized using polypyrrole (PPy), a natural amino acid, to graft Hg(II) and azo dyes onto the surface of the nanocomposite, and (3) immobilization of meso-tetrakis (4-carboxyphenyl) porphyrin based on Fe_3O_4/PPy core-shell by a facile route. To recluse investigation of the ratio effect of core and shell amounts, the adsorbent was prepared with two different percentages: 2.53 and 33. In this work, some critical factors on the efficiency of adsorbent have been studied, including concentration and time. Structural and morphological changes induced by modification were confirmed by X-ray diffraction, Fourier transforms infrared, scanning electron microscopy, and energy-dispersive X-ray spectroscopy analysis. UV-visible (UV-vis) spectra illustrate the elimination percentages of methylene blue (MB) and methyl orange (MO). Inductively coupled plasma analysis was used to investigate the removal of Hg(II) ions. The results illustrated that the adsorbent shows efficiency up to 100%. Furthermore, UV-vis spectroscopy was used to show that the prepared nanocomposite removes MB and MO dyes with a yield of 100% and 95%, respectively. The porous structure was also investigated by Brunauer–Emmett–Teller analysis, and a type VI isotherm was obtained. The magnetic nanocomposite is featured with superparamagnetism, excellent reusability, and a high anti-interfering ability to remove Hg(II) toxic ions and organic pollutants such as MB and MO in an aqueous medium at room temperature.

Keywords: Polypyrrole; Functionalized polymer; Adsorption; Hg(II); TCPP

1. Introduction

Mercury, a well-known toxic heavy metal, has attracted increasing attention because of its persistence in human and other creatures' food chains. Hence, it is considered a high-level global threat regarding public health and the environment [1]. Mercury can be produced from various natural and mankind sources. Its most common sources include oceanic and volcanic emissions, fossil fuel combustion, gold mining, drugs or cosmetics, chemical industry, and electronic manufacturing, which lead to the release of this harmful metal to water and soil. There are two

* Corresponding author.

1944-3994/1944-3986 © 2021 Desalination Publications. All rights reserved.

oxidation states for mercury: Hg(I) and Hg(II). Hg(I) compounds are not prevalent, and most of their compounds appear as Hg(II). Hg(II) is the common inorganic form of mercury in both anthropogenic effluents. Its higher toxicity than other mercury ions is due to its converting to other dangerous organic forms via biological methylation [2]. Due to the high toxicity of this heavy metal, the World Health Organization (WHO) has set some limits for human consumption. The maximum acceptable level of Hg for human consumption is 0.3 mg per week and less than 0.002 mg/L (2 ppb) in drinking water [3].

Nevertheless, developing highly efficient methods for the removal of mercury from wastewaters is essential. Also, heavy metals are not only wastewater pollutants, and the existence of azo dyes as a contaminant agent is not negligible. The main feature of this kind of dyes is the –N=N– group in their structures. Azo is a famous class of dyes produced in many industries and used in textile, food, leather, paper, plastic, and cosmetic manufacturing [4]. Annually, it has been estimated that 2.8 × 105 tons of textile dyes are discharged in corresponding industrial effluents [5]. Among different kinds of azo dyes, methylene blue (MB) and methyl orange (MO) are dominantly used. Finding an effective and inexpensive method for removing these dyes can be very useful for improving the quality of life.

Some specific techniques have been used for eliminating each Hg(II) and azo dye contamination in aqueous solutions. The conventional methods used to extract Hg(II) from waste include chemical precipitation, physical process, phytoextraction, ion exchange, ultrafiltration, reverse osmosis, and both electrodialysis and electrochemical recovery. Furthermore, coagulation, flocculation, precipitation, membrane filtration, electrochemical techniques, and conventional biological treatment methods are used to treat the azo dyes. However, these technologies are not entirely effective because most of them require large land areas and are quite expensive [6,7]. Compared with other techniques, the adsorption process has received considerable attention because of its low cost, high efficiency, simple feature to operate, and reversibility [8]. Many kinds of adsorbents have been used for the removal of pollutants from wastewater, such as activated carbon [9], clays [10], chelating resin [11], cellulose [12], zeolites [13], and silica gel [14]. The synthesis of suitable adsorbents with a strong association and high loading capacity is still a significant challenge. The convenient separation from water is considered a valuable advantage for adsorbents. Therefore, magnetic ones have drawn extensive attention during the early years [15].

Because of the unique properties and potential applications of the nanostructures magnetic materials in color imaging, ferrofluids, magnetic recording media, catalysts, advanced magnetic materials, and medical diagnostics [16–18], they have attracted much attention over the past decades. As a representative example, Fe_3O_4 is widely exerted due to its strong magnetic properties as well as its fast and facile preparation method [19,20]. On the other hand, polypyrrole (PPy), as a typical soft polymer, was found to be a highly efficient absorbent due to its rich functional groups. That polymer illustrated good adsorption performance for heavy metal ions [21] PPy can significantly improve cycling performance and rate capability by avoiding the dissolution and aggregation of nanomaterials, especially magnetic ones.

Magnetic polymer compounds that benefit from both magnetic nanoparticles and polymers are ideal candidates for pollutant adsorption [22]. Fe_3O_4, as a useful magnetic nanoparticle, has the potential to become an ideal adsorbent due to its chemical stability, biocompatibility, uniform structure, and large surface area [23]. However, pure Fe_3O_4 magnetic nanoparticles are easily agglomerate. Their chemical stability is weak and functional groups are few. So, their direct application confronts some problems in wastewater treatment [24]. In recent years, magnetic polymer composites such as MCC@NGO [25], G-g-C@NF [26], and CF@SS@PTG [27] have been applied to remove heavy metal ions and azo dyes from wastewater. These adsorbents show high adsorption capacity and magnetically separable properties, but their significant defect is that they are only effective under acid conditions, limiting their practical application.

Nowadays, fabrication of inorganic/organic core-shell nanostructures and nanocomposites with desired are prepared as they combine two different materials to produce functional composite materials and improve their properties [28–31]. Functional core-shell heterostructure, integrating the properties of multiple components, has been intensively explored in the fields such as catalysts, energy storage systems [32,33] biosensors [34], and absorption [35,36]. Both components' synergic absorption effects can lead to making a capable adsorbent.

In this work, for the first time, we synthesis a novel Fe_3O_4@ppy core-shell adsorbent, which tetrakis (4-carboxyphenyl) porphyrin (TCPP) modifies. For proper investigation of adsorbent, two steps optimization has been carried out. One is the preparation of adsorbent with two different molar ratios and comparing their efficiency, and the second is the immobilization of TCPP, as an excellent adsorbent, on the surface of nanostructured core-shell. The mechanism of Hg(II) elimination is shown in Fig. 1. Our main aim was to design and prepare a high-efficiency nanocomposite absorbent to remove heavy metal ions and azo dyes. Hg(II), MB, and MO were chosen as common water pollutants in this study.

2. Experimental

2.1. Materials and characterization

The azo dyes MO (molecular formula: $C_{14}H_{14}N_3NaO_3S$), MB (molecular formula: $C_{16}H_{18}ClN_3S$), and Mercury(II) nitrate, as the source of Hg(II) ions, were used as model water-soluble compounds. All solvents and reagents for the syntheses were of analytical grade and were used as received from commercial sources without further purification. X-ray diffraction (XRD) patterns were recorded on a JEOL powder X-ray diffractometer with monochromatic Cu Kα radiation (λ = 1.5418 A). In order to investigate of core-shell images, scanning electron microscopy (SEM) was obtained on a VEGA/TESCAN with an accelerating voltage of 30.00 kV. Fourier transform infrared (FT-IR) spectra were collected on a Shimadzu FTIR-8400S spectrophotometer using a KBr pellet for sample preparation (Shimadzu, Japan). The FT-IR spectra were recorded over the range of 4,000–400 cm^{-1}.

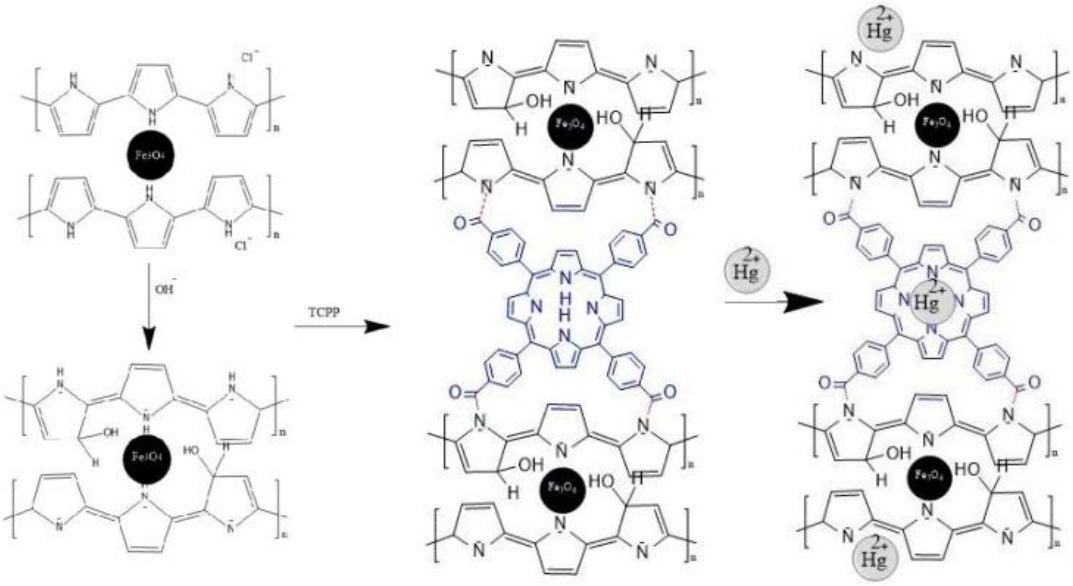

Fig. 1. Mechanism of TCPP/Fe_3O_4@PPy adsorbent for removal of Hg(II).

The Brunauer–Emmett–Teller (BET) method was utilized to calculate the specific surface areas (SBET). To evaluate the pore size distributions (PSDs), the Barrett–Joyner–Halenda (BJH) method was used. Mesopore area and mesopore volume were determined by the *t*-plot route. The samples were degassed at 76 K for 10 h before recording the nitrogen sorption isotherms. To determine Hg(II) ion removal by the adsorbent, the residual Hg(II) concentration was determined using an inductively coupled plasma atomic emission spectrophotometer (ICP-AES Atomscan advantage).

2.2. Synthesis of Fe_3O_4 nanoparticles

The preparation of magnetic Fe_3O_4 nanoparticles was performed by the chemical co-precipitation approach [27]. To synthesize Fe_3O_4 nanoparticles, homogeneous in size, and composition, it is important to perform the reaction in an aqueous solution with a molar ratio of Fe(II)/Fe(III) = 0.5 and a pH = 11–12. In a typical synthesis, 1.28 mol of $FeCl_3{\cdot}6H_2O$, and 0.64 mol $FeCl_2{\cdot}4H_2O$ were dissolved in 75 mL deionized water in a 150 mL three-necked Erlenmeyer flask, a nitrogen inlet under mechanical stirring. The mixture was stirred under N_2 at a rate of 800 rpm to form a clear solution and the process was followed by dropwise addition of 40 mL 15 M ammonia aqueous solution. The last step generated an instant black precipitate. The paramagneticity was checked *in situ* by placing a magnet near the black precipitate of Fe_3O_4. The reaction was allowed to proceed at 50°C for 6 h under inert N_2. The reaction mixture was cooled at room temperature and centrifuged at 3,000 rpm to collect a black precipitate. Finally, the obtained black particles were rinsed with deionized water to remove excess ions until neutrality and then dried in an oven at 80°C for 24 h.

2.3. Preparation of Fe_3O_4@PPy (FP) core-shell

The obtained Fe_3O_4 nanoparticles from the previous step were dispersed in 50 mL deionized water under sonication for 15 min. At the next step, 175 mmol of $FeCl_3{\cdot}6H_2O$ were then added to this mixture under vigorous stirring for 30 min until the $FeCl_3$ dissolved and the mixture temperature was stabled at –5°C by an ice bath. Then, pyrrole (17.3 mmol) was added dropwise to the solution over 0.5 h. The addition time of pyrrole is very important because it plays a decisive role in the polymerization process. Finally, the black product was collected with the help of a magnet, washed several times with distilled water repeatedly to remove the residual pyrrole monomers, and then dried in a vacuum oven for 24 h. In order to alkalization of Fe_3O_4@PPy core-shell, firstly, 0.5 g of core-shell was dispersed in distilled water and the amount of pH was measured (pH = 2.46). Under the sonication process, the solution of NaOH was added up to pH reached 12. With help of a magnetic field, the resulting black precipitation was collected and the product was vacuum-dried at 70°C for 24 h [37]. In fact, alkalization of core-shell nanostructures could prepare their surfaces for a high-efficiency modifying process.

2.4. Preparation of Fe_3O_4@PPy/TCPP nanocomposites

To functionalize Fe_3O_4@ppy core-shell with TCPP, the PPy/Fe_3O_4 nanocomposite was treated with NaOH. Briefly, PPy/Fe_3O_4 nanocomposites were titred with NaOH (2 M) solution till pH = 12 and maintained at 100°C for 1 h. The immobilization of TCPP particles on the surface of nanocomposite has been performed by the reflux method in DMF for 3 h. That process was carried out with the addition of 0.88 mmol of TCPP and 0.5 g of nanocomposite into the DMF solution. The final product was washed several times with ethanol and dried in the oven at 40°C for 5 h [38].

3. Results and discussion

SEM images of FPT (2.53%) and FPT (33%) compounds are displayed in Fig. 2A and B, respectively. As shown in

Fig. 1, the FPT (2.53%) has bulk morphology with a particle size of about 300 nm whereas the morphology of FPT (33%) is spherical with a particle size of 200 nm. Because of a low percentage of Fe_3O_4 in FPT (2.53%), the nucleariza-tion process has been defectively done, so the particles are agglomerated. In Fig. 2B, compared with Fig. 2A, a shell around the core is shown, and the spherical morphology of the FPT (33%) became more explicit. The corresponding energy-dispersive X-ray spectroscopy (EDS) spectrum and elemental composition are shown in Fig. 2C and D. According to elemental analysis, it is clear that both compounds are synthesized with expected elementary percentages.

To confirm the formation of Fe_3O_4, PPy, and TCPP, all three samples (1, 2, and 3) were characterized by FT-IR spectroscopy. As shown in Fig. 3, the sample 1 spectrum has exhibited the peaks at 1,556 and 1,473 cm^{-1} correspond to C=C asymmetric and symmetric ring-stretching vibrations [39]. The broad peak centered around 3,410 cm^{-1}, and the other peaks at 1,630; 893; and 793 cm^{-1} arise from the stretching, bending, and deforming vibrations of O–H due to the surface adsorbed water and ethanol [42]. The peak at 1,315 cm^{-1} is attributed to C–N stretching vibration. The peaks at 1,191; 1,095; 926 cm^{-1} relate to in-plane and out-of-plane C-H and N–H bending vibrations, which revealed PPy polymerized on Fe_3O_4 [40,41].

Compared with the Fe_3O_4@ppy sample, with the addition of TCPP, the peak appears around 3,400–3,600 cm^{-1} that is

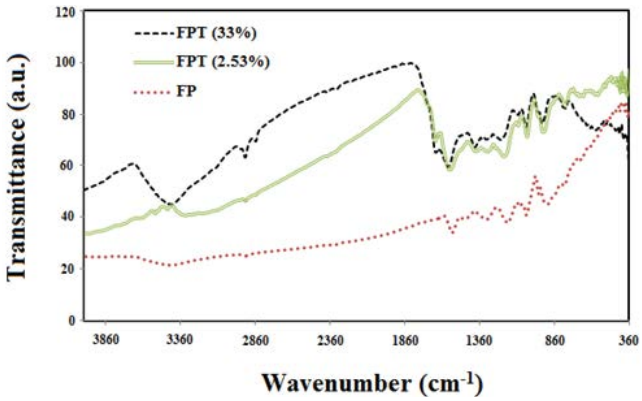

Fig. 3. FT-IR spectra of FP, FPT (2.53), and FPT (33%).

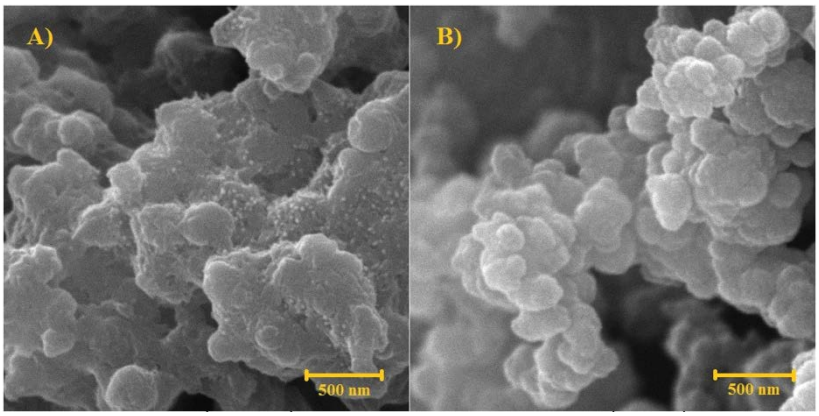

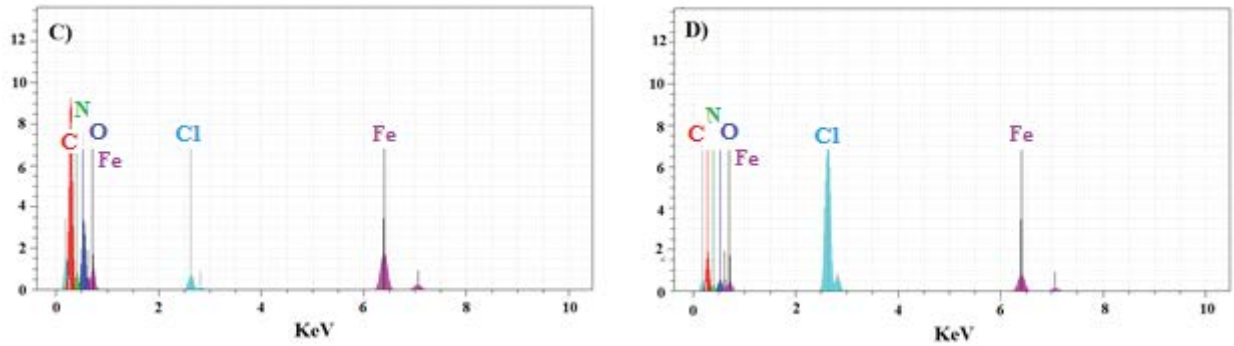

Element	Series	Unn C [Wt. %]	norm C [Wt. %]	Atom C [At. %]
Carbon	K series	30.71	31.78	46.34
Nitrogen	K series	12.81	13.26	16.58
Oxygen	K series	24.18	25.02	27.39
Chlorine	K series	1.67	1.71	0.84
Iron	K series	27.28	28.23	8.85

Element	Series	Unn C [Wt. %]	norm C [Wt. %]	Atom C [At. %]
Carbon	K series	23.39	23.34	4.07
Nitrogen	K series	13.04	13.01	19.16
Oxygen	K series	11.93	11.91	15.35
Chlorine	K series	29.81	29.75	17.30
Iron	K series	22.03	22.99	8.12

Fig. 2. (A and B) SEM images of Fe_3O_4@PPy and TCPP/Fe_3O_4@PPy nanocomposites and (C and D) the element analysis of both nanocomposites by EDS.

attributed to the O–H stretching vibration of absorbed water on the surface of the sample and observed peaks at 3,300 and 3,400 cm^{-1} in the spectra of TCPP/$FeWO_4$@RGO nanocomposite is for N–H vibration and O–H bond of carboxyl acid group in TCPP, respectively.

The X-ray powder diffraction technique confirmed the crystal structures of all the as-prepared samples, and the results are shown in Fig. 4. The first two patterns show the XRD pattern of sample 1 and modified sample 1 compounds (FP and FPT 2.53%). It can be seen, the sample 1 pattern is amorphous, but with modifying of sample 1 surface with TCPP particles, sharp peaks appear. The appearance of these peaks is a good reason for the embedding of TCPP particles between polymeric chains and consists of a sandwich-like structure. In the next two patterns (FP and FPT 33%), the crystalline structure of sample 2 in the presence and without TCPP are illustrated. Unlike sample 1, sample 2 exhibits sharp peaks, but the addition of TCPP is caused to increasing peaks intensity and some redundant peaks eliminated. Therefore, the placement of TCPP into polymer structure improves the crystallinity of the compound and makes clear and sharp peaks.

BET analysis was used to investigate the porous structure of compounds. The porous feature of the Fe_3O_4@ppy was evaluated by the BET method, and the obtained results illustrated that the BET surface area of Fe_3O_4@ppy is 461.34 m^2/g, a total pore volume is 0.39 m^3/g with a pore size of 9.5 nm while for Fe_3O_4@ppy/TCPP compound, the total pore volume would be triple, and pore size is decreased (Table 1).

3.1. Effect of amount of adsorbent, time, and concentration on the removal of Hg(II)

In Fig. 5, the influences of the amount of adsorbent on the removal percentage of an aqueous solution of 50 ppm Hg(II) were investigated. For this purpose, the amount of both samples 1 and 2 varies between 0 and 2 g/L. Furthermore, all experiments were done under pH = 4.46 as an optimum condition. The results show that the increase in the amount of 0–0.75 g/L can be affected by Hg(II) elimination. According to obtained results, the optimum amount for the removal process was determined 0.75 g/L. The effect of time is the difference for the two above samples when TCPP is added to the adsorbent structures. The modified sample with TCPP reaches maximum removal percentage (100%) at 15 min, but the pure sample's optimum time is about 18 min with only 50% removal efficiency. There are the same conditions for sample 2 and modified only difference because sample 2 removal efficiency is negligibly raised: 58%. The presence of TCPP had three positive results on reaction efficiency: (1) increasing of dispersing property and so more collision between mercury ions and adsorbents, (2) nitrogen atoms in the tetrapyrrole ring act as ligand sites and adsorb metal ions through the formation of nitrogen-metal coordination bonds, and (3) growth of porosity with the addition of TCPP (according to BET results). For evaluation of concentration factor, a series of experiments were accomplished at a concentration of 10, 20, 50, and 100 mg/L. The results indicated in Figs. 6 and 7 show that the Hg(II) removing efficiency for both modified samples is constant at 100% at 0–50 mg/L. After that, the amount of Hg(II) gradually falls. For samples 1 and 2, Hg(II) concentration rapidly decreased in the medium in the range of 0–20 mg/L, and the elimination percentage curve is decreasing, although that reduction for sample two is more intense. To conclude, because of the lack of enough

Table 1
Comparison of obtained BET analysis results for FP and FPT nanocomposites

Adsorbent	Fe_3O_4@ppy	Fe_3O_4@ppy/TCPP
Surface area (m^2/g)	461.34	532.25
Pore volume (m^3/g)	0.39	0.96
Pore size (nm)	9.5	8.2

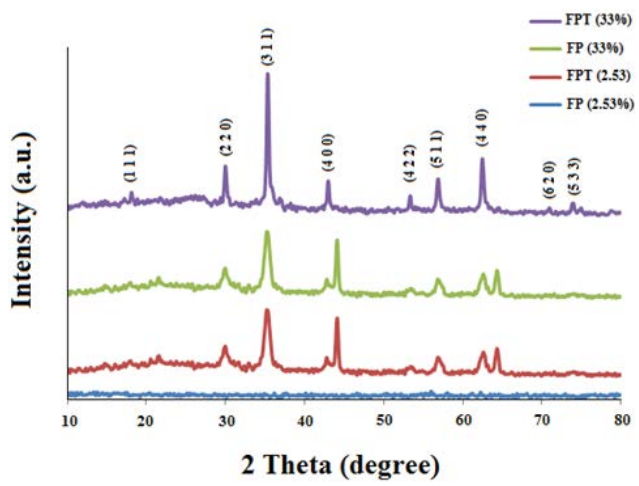

Fig. 4. XRD pattern of FP (2.53%), FPT (2.53%), FP (33%), and FPT (33%) nanocomposites.

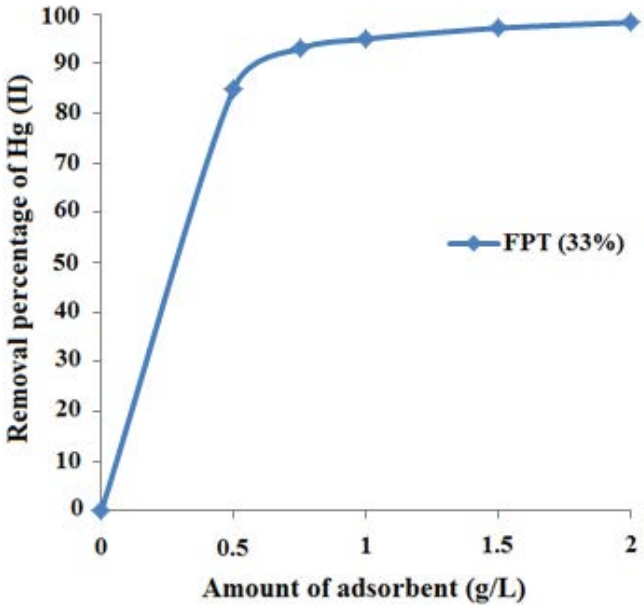

Fig. 5. Effect of amount of FPT (33%) adsorbent on removal efficiency of Hg(II).

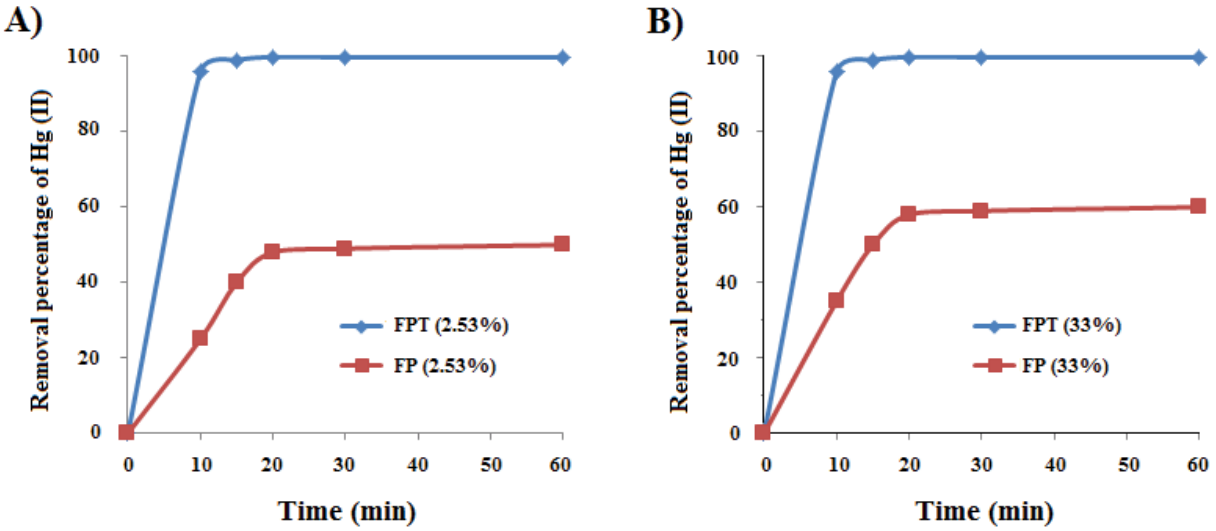

Fig. 6. Effect of time on removal efficiency of Hg(II) for (A) FP and FPT (2.53) and (B) FP and FPT (33%).

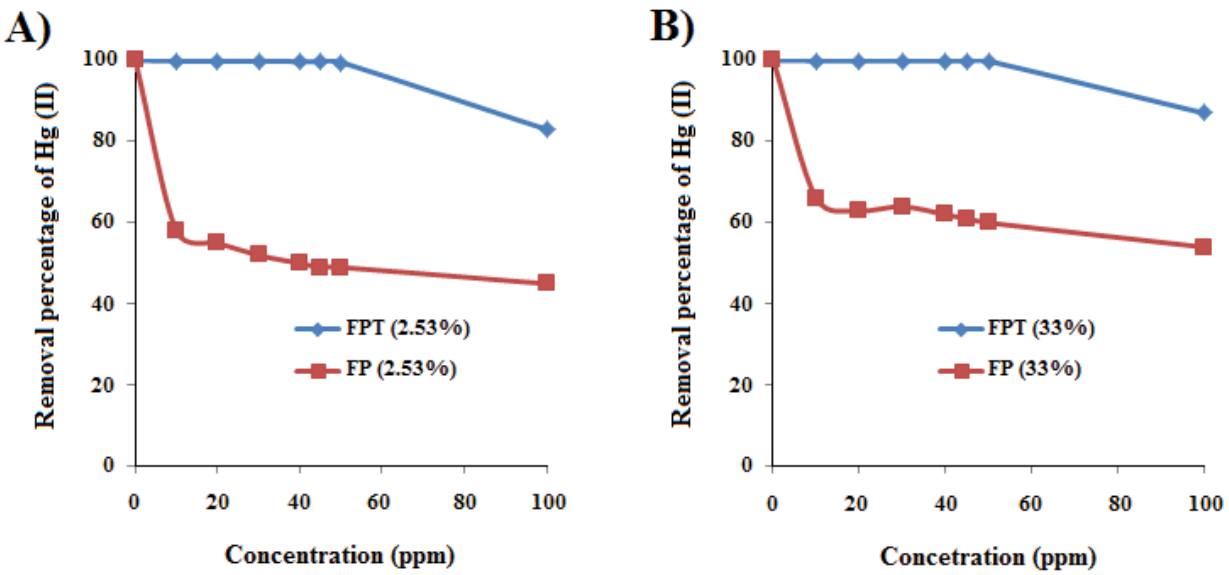

Fig. 7. Evaluation of the effect of concentration effect on removal efficiency of Hg(II) for (A) FP and FPT (2.53) and (B) FP and FPT (33%).

vacant sites for Hg(II) in higher concentrations, removal efficiency is logical. In the present study, Hg(II) were used with a concentration of 10, 20, 30, 40, 45, 50, and 100 mg/L. Also, for these tests, a constant weight of 37.5 mg of adsorbent was used. The experiments were programmed to evaluate the influence of six adsorbate/adsorbent mass ratios (mg/g) and obtained results for above concentration were 0.013, 0.026, 0.040, 0.052, 0.058, 0.066, and 0.133, respectively.

3.2. Effect of time and concentration on the removal of MB and MO

The contact time necessary to reach equilibrium depends on the initial dye concentration. It has been shown that the adsorption capacity increases with this concentration, and the rate of adsorption on the surface should be proportional to a driving force times an area. The effect of contact time on the performance of nanocomposites in adsorbing azo dyes was examined in the range of 1–60 min using the following parameters (temperature = 298 K; C_0 = (10, 20, 30, 50, and 100 mg/L); pH = 4.46; adsorbent dose = 37.5 mg). Fig. 8a and b show the effect of the time factor on the percentage of removal of MB from 50 ppm solution by four different samples. Here, removing MB dyes is done quickly, and with increasing time, the amount of dye removal also increases. The maximum elimination time is about 20 min, and the equilibrium time is about 45 min. The results indicated that the TCPP has an effective role in yield efficiency due to its high adsorption property. The modified core-shell performance enables a rapid initial uptake, with equilibrium reached in less than 5 min. The effect of MC concentration on MB and MO adsorption

at a contact time of 1 h was studied using a range of the adsorbent from 0 to 0.1 g L^{-1} in a 10 mg L^{-1} MB solution. As seen in Figs. 9 and 11, increasing the nanocomposite concentration is thus seen to improve the percentage removal of pollutants. Increased adsorbent concentration relates to a greater surface area of TCPP and, consequently, many possible active sites. For MO, the same process is carried out, but removal yield declines from 95% to 90%. The obtained results from an investigation of concentration factors illustrated that sample 1 experienced a more dramatic decrease, falling to about 30% in 10 ppm, and then had a steady trend from 10 to 50 ppm. The elimination percentage declined at a steady rate to under 20%. Finally, the yield of adsorbent for Hg(II) and azo dyes were included with other studies in Table 2, and results indicated that the as-prepared nanocomposite is a more effective adsorbent than others. In order to evaluation of adsorbate/adsorbent mass ratios (mg/g), adsorbate concentration of 10, 20, 30, 50, and 100 mg/L was used with a constant weight of 37.5 mg of adsorbent. The mass ratios (mg/g) were, respectively, acquired 0.013, 0.026, 0.040, 0.066, and 0.133 which is indicated appropriated adsorption capacity.

3.3. Reusability of the adsorbent

The reusability of the adsorbent has great importance from both industrial and environmental points of view. This property of the adsorbent is shown in Fig. 12. After each reaction, the catalyst was separated by the magnetic field, washed three times with solvent, dried at 60°C, and reused for the following fresh reaction under the same reaction conditions. The results indicated that the recovered FPT (33%) adsorbent, as the compound with the highest removal activity, can be used for four runs without significant loss of its activity.

4. Conclusions

A magnetic Fe_3O_4@PPy core-shell was decorated with TCPP (Fe_3O_4@PPy/TCPP) using a simple room temperature protocol. In this green synthesis route, the polymer matrix and TCPP particles played an essential role in removing toxic Hg(II), MB, and MO dyes from wastewater. The formation of PPy on the magnetic core was confirmed by SEM, XRD, and BET analyses. Moreover, immobilization of TCPP on the surface of the core-shell was also confirmed by the FT-IR study. TCPP was embedded and nicely decorated on the surface of the magnetic nanocomposite. The as-prepared adsorbent exhibited excellent activity toward eliminating Hg(II) ions and dyes in the presence of NaOH as a reductant agent. Also, the amount of adsorbent, time, initial concentration, factors for removing Hg(II), and time and concentration factors for eliminating MB and MO dyes are investigated. In each case, the modified core-shells (33%) by TCPP indicated more efficiency. The results showed that in the case of Hg(II), increasing the amount of the optimal adsorbent (FTP (33%)) by 0.5 g and the time by more than 10 minutes increases the reaction efficiency by more than 90% with a gentle slope of about 100%, and in concentrations higher than 50 ppm, the reaction yield is decreased

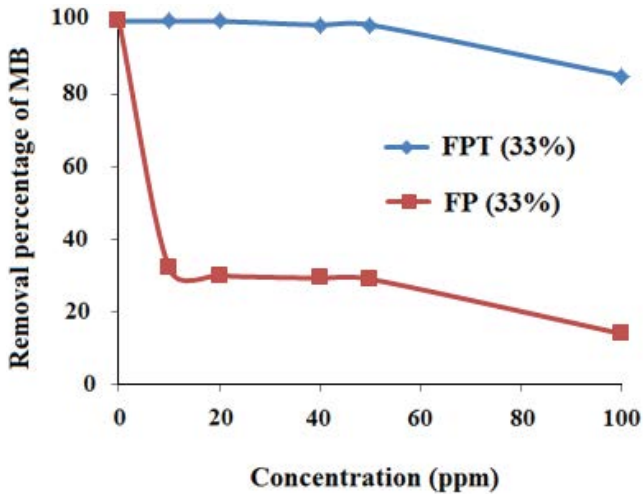

Fig. 9. Effect of nanocomposites concentration on MB adsorption.

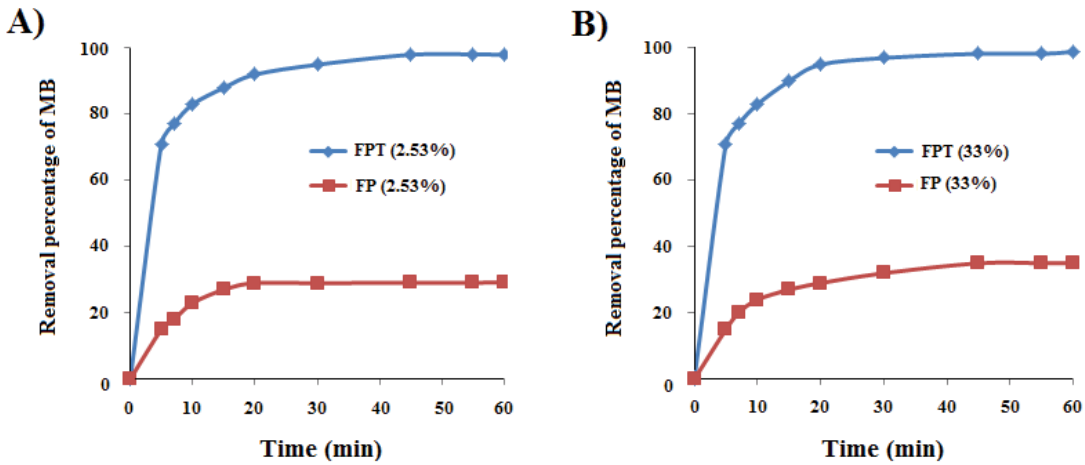

Fig. 8. (A and B) Effect of contact time on the adsorption of MB onto samples and the percentage of MB removed at initial MB concentrations at room temperature.

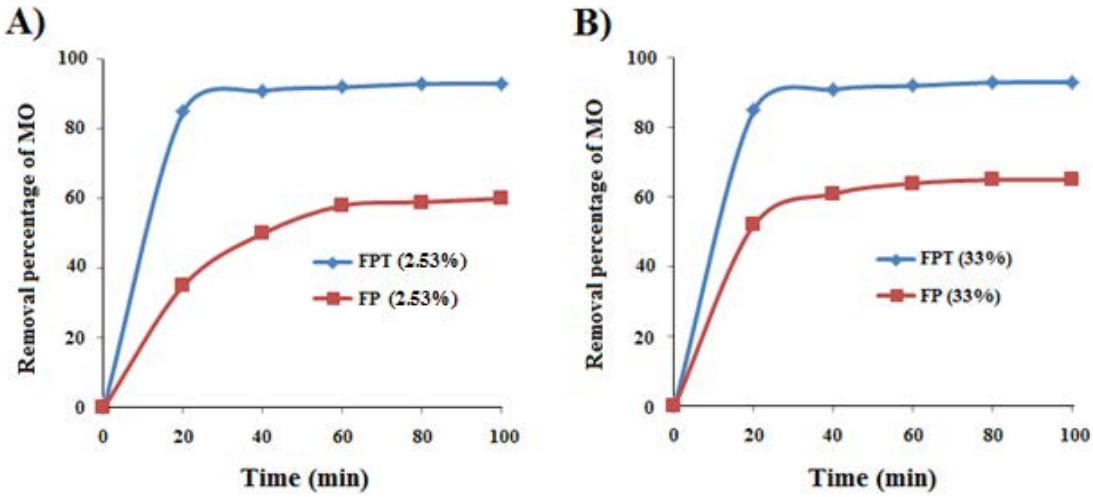

Fig. 10. (A and B) Effect of contact time on the adsorption of MO onto nanocomposites and the percentage of MO removed at initial MO concentrations at room temperature.

Table 2
Removal of azo dyes OR Hg(II) pollutants benzaldehyde by adsorbent in the presence of various catalysts

Adsorbent	Time (min)	Pollutant	Yield (%)	Ref.
meth-CNF	90	Hg(II)	90	[42]
AF-PANF	120	Hg(II)	99	[43]
PANI-KpF	1,440	MO	68	[44]
DMG-AMB	480	MB	22.5	[45]
Fe_3O_4@PPy/TCPP	60	Azo dye, Hg(II)	100, 95	This work

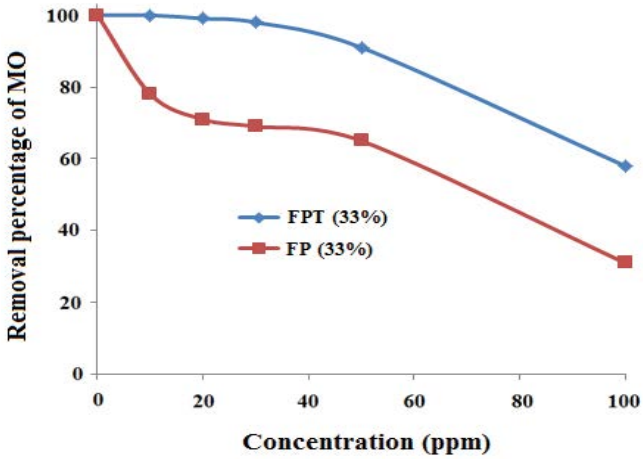

Fig. 11. Effect of nanocomposites concentration on MB adsorption.

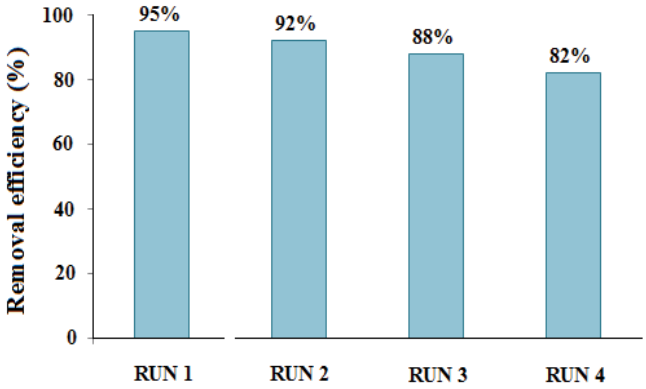

Fig. 12. Reusability of FPT (33%) adsorbent nanocomposite in the elimination of MB.

by less than 20%. The same trends were carried out for the elimination of azo dye with some minor changes.

References

[1] D. Malakoff, Taming a Mercurial Element, American Association for the Advancement of Science, 2013.
[2] Q. Wang, D. Kim, D.D. Dionysiou, G.A. Sorial, D. Timberlake, Sources and remediation for mercury contamination in aquatic systems—a literature review, Environ. Pollut., 131 (2004) 323–336.
[3] T.A. Saleh, M. Tuzen, A. Sarı, Polyamide magnetic palygorskite for the simultaneous removal of Hg(II) and methyl mercury; with factorial design analysis, J. Environ. Manage., 211 (2018) 323–333.
[4] M. Rafatullah, O. Sulaiman, R. Hashim, A. Ahmad, Adsorption of methylene blue on low-cost adsorbents: a review, J. Hazard. Mater., 177 (2010) 70–80.
[5] O.A. Sofola, P. Jin, Y. Qin, R. Duan, H. Liu, M. de Haro, D.L. Nelson, J. Botas, RNA-binding proteins hnRNP A2/B1 and Cugbp1 Suppress Fragile X CGG premutation repeat-induced

neurodegeneration in a Drosophila model of FXTAS, Neuron, 55 (2007) 565–571.
[6] R. Kumar, R. Ahmad, Biosorption of hazardous crystal violet dye from aqueous solution onto treated ginger waste (TGW), Desalination, 265 (2011) 112–118.
[7] Z. Beiramzadeh, M. Baqersad, M. Aghababaei, Application of the response surface methodology (RSM) in heavy metal removal from real power plant wastewater using electrocoagulation, Eur. J. Environ. Civ. Eng., (2019) 1–19, doi: 10.1080/19648189.2019.1640139.
[8] F. Ke, L.G. Qiu, Y.P. Yuan, F.M. Peng, X. Jiang, A.J. Xie, Y.H. Shen, J.F. Zhu, Thiol-functionalization of metal-organic framework by a facile coordination-based postsynthetic strategy and enhanced removal of Hg^{2+} from water, J. Hazard. Mater., 196 (2011) 36–43.
[9] F.D. Natale, A. Erto, A. Lancia, D. Musmarra, Mercury adsorption on granular activated carbon in aqueous solutions containing nitrates and chlorides, J. Hazard. Mater., 192 (2011) 1842–1850.
[10] T. Phothitontimongkol, N. Siebers, N. Sukpirom, F. Unob, Preparation and characterization of novel organo-clay minerals for Hg(II) ions adsorption from aqueous solution, Appl. Clay Sci., 43 (2009) 343–349.
[11] R.J. Qu, C.M. Sun, Y. Zhang, J. Chen, C.H. Wang, C.N. Ji, X.G. Liu, Syntheses, Characterization, and Hg(II) adsorption properties of porous cross-linked polystyrene modified with 2-aminopyridine via a sulfoxide/sulfone-containing spacer arm, J. Chem. Eng. Data, 55 (2010) 4343–4351.
[12] Y.M. Zhou, X.Y. Hu, M. Zhang, X.F. Zhuo, J.Y. Niu, Preparation and characterization of modified cellulose for adsorption of Cd(II), Hg(II), and acid fuchsin from aqueous solutions, Ind. Eng. Chem. Res., 52 (2013) 876–884.
[13] X.Y. Zhang, Q.C. Wang, S.Q. Zhang, X.J. Sun, Z.S. Zhang, Stabilization/solidification (S/S) of mercury-contaminated hazardous wastes using thiol-functionalized zeolite and Portland cement, J. Hazard. Mater., 168 (2009) 1575–1580.
[14] K.S. Xia, R.Z. Ferguson, M. Losier, N. Tchoukanova, R. Brüning, Y. Djaoued, Synthesis of hybrid silica materials with tunable pore structures and morphology and their application for heavy metal removal from drinking water, J. Hazard. Mater., 183 (2010) 554–564.
[15] S.C.N. Tang, I.M.C. Lo, Magnetic nanoparticles: essential factors for sustainable environmental applications, Water Res., 47 (2013) 2613–2632.
[16] Z. Xiu, J. Ma, X. Wang, Z. Gao, X. Meng, Hierarchical porous Fe_3O_4@N-doped carbon nanoellipsoids with excellent electrochemical performance as anode for lithium-ion batteries, J. Solid State Chem., 282 (2020) 121118, doi: 10.1016/j.jssc.2019.121118.
[17] X. Teng, H. Yang, Effects of surfactants and synthetic conditions on the sizes and self-assembly of monodisperse iron oxide nanoparticles, J. Mater. Chem., 14 (2004) 774–779.
[18] A.C.C. Yu, M. Mizuno, Y. Sasaki, H. Kondo, K. Hiraga, Structural characteristics and magnetic properties of chemically synthesized copt nanoparticles, Appl. Phys. Lett., 81 (2002) 3768–3770.
[19] M. Moshari, M. Rabbani, R. Rahimi, Synthesis of TCPP–Fe_3O_4@S/RGO and its application for purification of water, Res. Chem. Intermed., 42 (2016) 5441–5455.
[20] A.Y. Louie, M.M. Hüber, E.T. Ahrens, U. Rothbächer, R. Moats, R.E. Jacobs, S.E. Fraser, T.J. Meade, *In vivo* visualization of gene expression using magnetic resonance imaging, Nat. Biotechnol., 18 (2000) 321–325.
[21] Y. Wang, B. Zou, T. Gao, X. Wu, S. Lou, S. Zhou, Synthesis of orange-like Fe_3O_4/Ppy composite microspheres and their excellent Cr(VI) ion removal properties, J. Mater. Chem., 22 (2012) 9034–9040.
[22] A. Kara, E. Demirbel, N. Tekin, B. Osman, N. Beşirli, Magnetic vinylphenyl boronic acid microparticles for Cr(VI) adsorption: kinetic, isotherm and thermodynamic studies, J. Hazard. Mater., 286 (2015) 612–623.
[23] Q. Zhang, Y.Q. He, X.G. Chen, D.H. Hu, L.J. Li, T. Yin, L.L. Ji, Structure and photocatalytic properties of TiO_2-graphene oxide intercalated composite, Chin. Sci. Bull., 56 (2011) 331–339.
[24] S. Chen, J. Zhu, X. Wu, Q. Han, X. Wang, Graphene oxide–MnO_2 nanocomposites for supercapacitors, ACS Nano, 4 (2010) 2822–2830.
[25] A.Z. Moghaddam, E. Esmaeilkhanian, M.S. Fard, Immobilizing magnetic glutaraldehyde cross-linked chitosan on graphene oxide and nitrogendoped graphene oxide as well-dispersible adsorbents for chromate removal from aqueous solutions, Int. J. Biol. Macromol., 128 (2019) 61–73.
[26] A.Z. Moghaddam, E. Ghiamati, A. Pourashuri, A. Allahresani, Modified nickel ferrite nanocomposite/functionalized chitosan as a novel adsorbent for the removal of acidic dyes, Int. J. Biol. Macromol., 120 (2018) 1714–1725.
[27] A.Z. Moghaddam, M.E. Jazi, A. Allahrasani, M.R. Ganjali, A. Badiei, Removal of acid dyes from aqueous solutions using a new eco-friendly nanocomposite of $CoFe_2O_4$ modified with tragacanth gum, J. Appl. Polym. Sci., 137 (2020) 48605, doi: 10.1002/app.48605.
[28] X. Yang, T. Dai, Y. Lu, Synthesis of novel sunflower-like silica/polypyrrole nanocomposites via self-assembly polymerization, Polymer, 47 (2006) 441–447.
[29] S. Pordel, M. Rabbani, R. Rahimi, M.H. Golafzani, A. Azad, Synthesis of mesoporous NiO/Bi_2WO_6 nanocomposite for selective oxidation of alcohols, Solid State Sci., 107, (2020) 106306, doi: /10.1016/j.solidstatesciences.2020.106306.
[30] J. Jang, J.H. Oh, Facile fabrication of photochromic dye–conducting polymer core–shell nanomaterials and their photoluminescence, Adv. Mater., 15 (2003) 977–980.
[31] S. Afshar, S. Pordel, B. Tahmouresilerd, A. Azad, Improving the photocatalytic activity of modified anatase TiO_2 with different concentrations of aluminum under visible light: mechanistic survey, Photochem. Photobiol., 92 (2016) 783–789.
[32] H. Zhang, D. Chen, X. Lv, Y. Wang, H. Chang, J. Li, Energy-efficient photodegradation of azo dyes with TiO_2 nanoparticles based on photoisomerization and alternate UV-visible light, Environ. Sci., 44 (2010) 1107–1111.
[33] Y. Ma, X. Wu, G. Zhang, Core-Shell Ag@Pt nanoparticles supported on sepiolite nanofibers for the catalytic reduction of nitrophenols in water: enhanced catalytic performance and DFT study, Appl. Catal., B, 205 (2017) 262–270.
[34] F.I. Hai, K. Yamamoto, K. Fukushi, Hybrid treatment systems for dye wastewater, Crit. Rev. Environ. Sci. Technol., 37 (2007) 315–377.
[35] C.A.M. Huitle, E. Brillas, Decontamination of wastewaters containing synthetic organic dyes by electrochemical methods: a general review, Appl. Catal., B, 87 (2009) 105–145.
[36] A.K. Gupta, A. Pal, C. Sahoo, Photocatalytic degradation of a mixture of crystal violet (Basic Violet 3) and methyl red dye in aqueous suspensions using Ag^+ doped TO_2, Dyes Pigm., 69 (2006) 224–232.
[37] X. Lu, H. Mao, W. Zhang, Fabrication of core-shell Fe_3O_4/polypyrrole and hollow polypyrrole microspheres, Polym. Compos., 30 (2009) 847–854.
[38] G. Huang, T. Su, K. Zeng, Y. Guo, S. Zhao, S. Wei, Mesoporous chitosan-immobilized iron tetrakis (4-carboxyphenyl) porphyrin as a model of cytochrome P-450 enzyme for oxidation of ethylbenzene, Appl. Organomet. Chem., 32 (2018) e4140, doi: 10.1002/aoc.4140.
[39] F. Han, D. Li, W.C. Li, C. Lei, Q. Sun, A.H. Lu, Nanoengineered polypyrrolecoated Fe_2O_3@C multifunctional composites with an improved cycle stability as lithium-ion anodes, Adv. Funct. Mater., 23 (2013) 1692, doi: 10.1002/adfm.201202254.
[40] T.F. Yi, L.Y. Qiu, J. Mei, S.Y. Qi, P. Cui, S. Luo, Y.R. Zhu, Y. Xie, Y.B. He, Porous spherical NiO@ $NiMoO_4$@PPY nanoarchitectures as advanced electrochemical pseudocapacitor materials, Sci. Bull., *65* (2020) 546–556.
[41] L.F. Cui, J.A. Shen, F.Y. Cheng, Z.L. Tao, J. Chen, SnO_2 nanoparticles@polypyrrole nanowires composite as anode materials for rechargeable lithium-ion batteries, J. Power Sources, 196 (2011) 2195, doi: 10.1016/j.jpowsour.2010.09.075.
[42] V. Bisla, G. Rattan, S. Singhal, A. Kaushik, Green and novel adsorbent from rice straw extracted cellulose for efficient adsorption of Hg(II) ions in an aqueous medium, Int. J. Biol. Macromol., 161 (2020) 194–203.

[43] S. Nasimi, M. Baghdadi, M. Dorosti, Surface functionalization of recycled polyacrylonitrile fibers with ethylenediamine for highly effective adsorption of Hg(II) from contaminated waters, J. Environ. Manage., 270 (2020) 110883, doi: 10.1016/j.jenvman.2020.110883.
[44] R.B. Gapusan, M.D.L. Balela, Adsorption of anionic methyl orange dye and lead(II) heavy metal ion by polyaniline-kapok fiber nanocomposite, Mater. Chem. Phys., 243 (2020) 122682, doi: 10.1016/j.matchemphys.2020.122682.
[45] A. Mekky, M.E. Masry, R. Khalifa, A. Omer, T. Tamer, Z. Khan, M. Gouda, M.M. Eldin, Removal of methylene blue dye from synthetic aqueous solutions using dimethylglyoxime modified amberlite ira-420: kinetic, equilibrium and thermodynamic studies, Desal. Water Treat., 181 (2020) 399–411.